



# ZnFe<sub>2</sub>O<sub>4</sub> multi-porous microbricks/graphene hybrid photocatalyst: Facile synthesis, improved activity and photocatalytic mechanism

Yang Hou<sup>a,b</sup>, Xinyong Li<sup>a,b,c,\*</sup>, Qidong Zhao<sup>a,b</sup>, Guohua Chen<sup>c</sup>

<sup>a</sup> Key Laboratory of Industrial Ecology and Environmental Engineering (MOE), School of Environmental Science and Technology, Dalian University of Technology, Dalian 116024, China

<sup>b</sup> State Key Laboratory of Fine Chemical, School of Environmental Science and Technology, Dalian University of Technology, Dalian 116024, China

<sup>c</sup> Department of Chemical and Biomolecular Engineering, The Hong Kong University of Science & Technology, Clear Water Bay, Kowloon, Hong Kong

## ARTICLE INFO

### Article history:

Received 27 February 2013

Received in revised form 25 April 2013

Accepted 28 April 2013

Available online 4 May 2013

### Keywords:

Zinc ferrite

Graphene

Multi-porous microbricks

Hybrid

Photocatalysis

## ABSTRACT

Great efforts have been made recently to develop graphene-based visible-light-response photocatalysts and investigate their application in environmental field. In this study, a novel graphene-supported ZnFe<sub>2</sub>O<sub>4</sub> multi-porous microbricks hybrid was synthesized via a facile deposition–precipitation reaction, followed by a hydrothermal treatment. The morphology, structure and optical properties of the hybrid were well characterized, indicating that an intimate contact between ZnFe<sub>2</sub>O<sub>4</sub> microbricks and graphene sheets has been formed. The photocatalytic degradation of p-chlorophenol experiments indicated that the graphene-supported ZnFe<sub>2</sub>O<sub>4</sub> multi-porous microbricks hybrid exhibited a much higher photocatalytic activity than the pure ZnFe<sub>2</sub>O<sub>4</sub> multi-porous microbricks and ZnFe<sub>2</sub>O<sub>4</sub> nanoparticles under the visible light irradiation ( $\lambda > 420$  nm). The enhancement of photocatalytic performance could be attributed to the fast photogenerated charge separation and transfer due to the high electron mobility of graphene sheets, improved light absorption, high specific surface area as well as multi-porous structure of the hybrid. Photoluminescence and radicals trapping studies revealed the hydroxyl radicals were involved as the main active oxygen species in the photocatalytic reaction. The work could open new possibilities to provide some insights into the design of new graphene-based hybrid photocatalysts with high activity for environmental purification applications.

© 2013 Elsevier B.V. All rights reserved.

## 1. Introduction

With the background of the increasing global air and water pollutions, semiconductor mediated photocatalysis has attracted considerable attention because it provides a promising pathway for solving energy supply and environmental pollution problems [1,2]. Of the semiconductors being developed as photocatalysts, TiO<sub>2</sub> is currently the most promising because of its special features, such as its low cost, non-toxicity and photochemical stability [3,4]. However, the band-gap of TiO<sub>2</sub> is too large (3.0–3.2 eV) so that it can only utilize solar energy of less than 5% [5,6]. Therefore, the development of novel visible-light-responsive photocatalysts with high activity is currently an intensive and hot research topic. In recent years, spinel ferrites are among the most studied materials and have been widely used in electronic devices [7], information storage

[8], magnetic resonance imaging [9], drug-delivery technology [10] and semiconductor photocatalysis [11–13]. Particularly, zinc ferrite (ZnFe<sub>2</sub>O<sub>4</sub>), a narrow-band-gap semiconductor (band-gap 1.9 eV), has been reported to be a promising visible-light-responsive photocatalyst [14,15]. It is well known that the properties of ZnFe<sub>2</sub>O<sub>4</sub> are strongly dependent on its morphology and microstructure. Thus, morphology controlled synthesis becomes an important issue. Many recent efforts have been directed toward the synthesis of ZnFe<sub>2</sub>O<sub>4</sub> micro-/nanostructures with diverse morphologies such as nanotubes [11,16], nanorods [12,17], nanofibers [18,19], micro-/nanospheres [14], microtimbers [20,21] and hollow spheres [22,23]. However, until now, a simple synthesis strategy for brick-like ZnFe<sub>2</sub>O<sub>4</sub> with a multi-porous structure is still rarely reported. The ZnFe<sub>2</sub>O<sub>4</sub> multi-porous microbricks (ZnFe<sub>2</sub>O<sub>4</sub>-MM) is expected to show improved performances in photocatalysis and energy conversion because of its unique structure.

Graphene, a new class of 2D carbonaceous material with atom-thick layer features, has attracted much attention recently for photoelectrochemical and photocatalytic applications due to its high specific surface area and fast electron transfer ability, which can effectively inhibit the recombination of the electron–hole pairs [24–26]. The unique electronic structures of both ZnFe<sub>2</sub>O<sub>4</sub> and

\* Corresponding author at: Key Laboratory of Industrial Ecology and Environmental Engineering (MOE), School of Environmental Science and Technology, Dalian University of Technology, Dalian 116024, China. Tel.: +86 411 8470 7733; fax: +86 411 8470 7733.

E-mail addresses: [xyli@dlut.edu.cn](mailto:xyli@dlut.edu.cn), [xinyongli@hotmail.com](mailto:xinyongli@hotmail.com) (X. Li).

graphene inspired us to design and synthesize graphene-supported  $\text{ZnFe}_2\text{O}_4$  hybrid. However, to date, relatively little attention has been concentrated on the construction of  $\text{ZnFe}_2\text{O}_4$ /reduced graphene oxide (RGO) nanocomposites [27–29] and there is no study focused on the utilization of the  $\text{ZnFe}_2\text{O}_4$ -MM/RGO hybrid as photocatalyst for water treatment. Hence, the development of graphene-supported  $\text{ZnFe}_2\text{O}_4$ -MM hybrid system and investigation of its photocatalytic activity is of fundamental and practical significance.

In this work, a novel  $\text{ZnFe}_2\text{O}_4$ -MM/RGO hybrid with high visible-light photocatalytic activity was synthesized via a facile deposition–precipitation reaction without use of any templates or surfactants, followed by a hydrothermal treatment. The promoting effect of the  $\text{ZnFe}_2\text{O}_4$ -MM/RGO hybrid on the photocatalytic activity was observed and the correlation between the structure and the property was discussed based on the results of a systematic characterization. A possible mechanism for the transfer of photogenerated carriers was also proposed.

## 2. Experimental

### 2.1. Synthesis of $\text{ZnFe}_2\text{O}_4$ -MM/RGO hybrid

All reagents were of commercially available analytical grade and were used without further purification.  $\text{ZnFe}_2\text{O}_4$ -MM was synthesized via a facile one-pot route. In a typical preparation, aqueous solutions of 0.1 M  $\text{ZnSO}_4 \cdot 7\text{H}_2\text{O}$  and 0.2 M  $\text{FeSO}_4 \cdot 7\text{H}_2\text{O}$  were prepared, respectively. A 100 mL aliquot of each solution was then mixed together at 80 °C. 300 mL 0.1 M  $(\text{NH}_4)_2\text{C}_2\text{O}_4$  solution was introduced into the above mixed solution and stirred for 30 min to produce  $\text{ZnFe}_2\text{O}_4$ -MM precursor. The precursor was further washed with distilled water several times and then dried at 100 °C for 1 h, followed by annealing in air at 500 °C for 2 h to obtain  $\text{ZnFe}_2\text{O}_4$ -MM.

$\text{ZnFe}_2\text{O}_4$ -MM/RGO hybrid was prepared by a hydrothermal method. Graphene oxide (GO) was synthesized through chemical exfoliation of graphite powder via a modified Hummers' method [30]. In a typical synthesis, 20 mg of GO was first dissolved in 40 mL of water by ultrasonic treatment for 1 h to obtain a suspension ( $0.5 \text{ mg mL}^{-1}$ ). Then, 0.2 g of the prepared  $\text{ZnFe}_2\text{O}_4$ -MM was added to the obtained GO solution and stirred for another 1 h to get a homogeneous suspension. After that, the suspension was transferred into a Teflon-lined autoclave and heated at 180 °C for 6 h to achieve reduction of GO. A dark red precipitate ( $\text{ZnFe}_2\text{O}_4$ -MM/RGO) resulted, which was centrifuged and then washed with distilled water and ethanol before being dried at 70 °C in air overnight.

### 2.2. Characterization

The morphology of  $\text{ZnFe}_2\text{O}_4$ -MM/RGO hybrid was characterized using a Tecnai T12 transmission electron microscope (TEM) and a Philips FEI XL30 field emission scanning electron microscope (FESEM) equipped with a PGT/IMIX PTS energy dispersive X-ray (EDX) system. The crystallinity of the sample was determined from XRD using a diffractometer with  $\text{Cu K}\alpha$  radiation (Shimadzu Lab-X XRD-6000). The accelerating voltage and applied current were 40 kV and 30 mA, respectively. Light absorption property was measured using UV–vis absorption spectra (JASCO, UV-550) with a wavelength range of 300–800 nm. Photoluminescence (PL) spectra were obtained on a Spex Fluorolog-3. All the spectra were taken at room temperature at excitation wavelength of 325 nm. Fourier transform infrared (FTIR) spectra were recorded on a Nicolet Nexus spectrometer with the standard KBr pellet method. A Dilor XY microspectrometer with 532 nm laser excitation was used to record the Raman spectra of the samples. Nitrogen adsorption–desorption

isotherm measurements were performed on a Quantachrome Autosorb 1 instrument to study specific surface area. Before analysis, all samples were pretreated by degassing at 200 °C for 8 h to remove any adsorbed species. Thermogravimetric analysis (TGA) was carried out using a TGA-Q500 thermoanalyzer with a heating rate of  $5^\circ\text{C min}^{-1}$  in air. X-ray photoelectron spectroscopy (XPS, PHI 5600 mode) was performed to examine the surface properties and composition of the sample. All the binding energies were calibrated by using the contaminant carbon (C 1s) 284.6 eV as a reference.

### 2.3. Photocatalytic activity test

Photocatalytic activity of the  $\text{ZnFe}_2\text{O}_4$ -MM/RGO hybrid was evaluated by degradation of p-chlorophenol (4-CP) in an aqueous solution. A 500 W Xenon lamp (Phillips) with a 420 nm edge filter was used as visible light resource ( $\lambda > 420 \text{ nm}$ ), and the average light intensity was about  $71.4 \text{ mW cm}^{-2}$ . Prior to irradiation, 80 mg of the  $\text{ZnFe}_2\text{O}_4$ -MM/RGO hybrid was dispersed in 100 mL of  $10 \text{ mg L}^{-1}$  4-CP aqueous solution, and the suspensions were put into a column-like container with magnetic stirring for 1 h in the dark to reach the absorption–desorption equilibrium. During the magnetic stirring, there was almost no aggregation induced by the magnetic effect between  $\text{ZnFe}_2\text{O}_4$ -MM/RGO hybrid and the magnetic stirrer because they had relative weak magnetic properties [27]. At given time intervals, 3 mL of the aliquots were sampled and analyzed by recording variations in the absorption band (224 nm) in the UV–vis spectra of 4-CP using a UV–vis spectrophotometer. Note that the measured absorption band of 4-CP at 224 nm might contain some contributions from small amounts of potential degradation intermediates of 4-CP, such as hydroquinone (absorption band centered at 288 nm) [31], benzoquinone (absorption band centered at 245 nm) [31], 4-chlorocatechol (absorption band centered at 283 nm) [32] and hydroxyhydroquinone (absorption band centered at 289 nm) [33]. The existence of degradation intermediates had little negative effect on the evaluation of photocatalytic activity [34–36]. We simplified the UV–vis absorption of those potential degradation intermediates to be the absorption by 4-CP at 224 nm approximately.

As a comparison, the photocatalytic activity of  $\text{ZnFe}_2\text{O}_4$  nanoparticles ( $\text{ZnFe}_2\text{O}_4$ -NP) was tested under the same experimental conditions [14]. The decrease in total organic carbon (TOC), which indicated the mineralization of 4-CP, was determined using a TOC analyzer (Shimadzu 5000A, Japan, T) at 650 °C equipped with an ASI5000 autosampler.

### 2.4. Analysis of hydroxyl radicals

The formation of hydroxyl radicals at the photoilluminated photocatalyst/water interface could be detected by a PL technique using terephthalic acid as a probe molecule [37]. Terephthalic acid readily reacted with hydroxyl radicals to produce highly fluorescent product, 2-hydroxyterephthalic acid. The intensity of the PL signal at 425 nm of 2-hydroxyterephthalic acid was in proportion to the amount of hydroxyl radicals produced in water. PL spectra of the generated 2-hydroxyterephthalic acid were measured on a Hitachi F-4500 fluorescence spectrophotometer. After light irradiation every 10 min, the reaction solution was filtrated to measure the increase of the PL intensity at 425 nm excited by 315 nm light.

## 3. Results and discussion

### 3.1. Structure and morphology properties of $\text{ZnFe}_2\text{O}_4$ -MM/RGO hybrid

The crystal structure of the  $\text{ZnFe}_2\text{O}_4$ -MM/RGO hybrid is characterized by XRD patterns, as shown in Fig. 1a. All of the diffraction

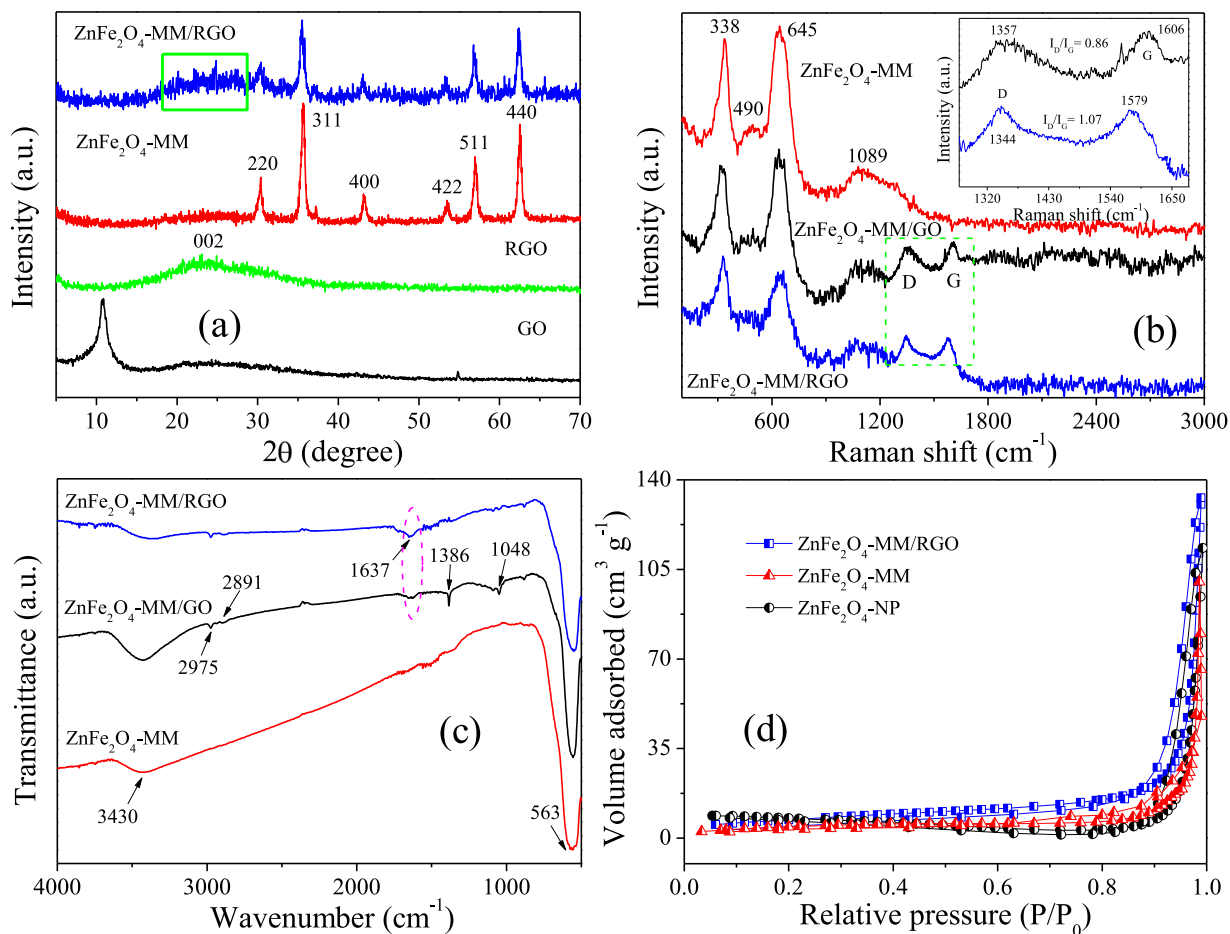


**Fig. 1.** XRD patterns (a), Raman spectra (b), FTIR spectra (c) and Nitrogen adsorption–desorption isotherm curves (d) of ZnFe<sub>2</sub>O<sub>4</sub>-MM and ZnFe<sub>2</sub>O<sub>4</sub>-MM/RGO hybrid. Additionally, data for GO, RGO, ZnFe<sub>2</sub>O<sub>4</sub>-NP and ZnFe<sub>2</sub>O<sub>4</sub>-MM/GO are also shown.

peaks of the hybrid can be readily indexed to the ZnFe<sub>2</sub>O<sub>4</sub> (JCPDS 22-1012) and graphene. The peaks at  $2\theta$  values of 30.4, 35.5, 43.0, 53.3, 56.9 and 62.4 can be attributed to (220), (311), (400), (422), (511) and (440) facets of spinel ZnFe<sub>2</sub>O<sub>4</sub>. Also, a broad and weak peak at  $2\theta$  value of 24.5 can be indexed to (002) plane of graphene, suggesting the reduction of GO to RGO sheets [38]. Note that we did not observe the diffraction peaks of other phases such as wurtzite structured ZnO and hematite phase Fe<sub>2</sub>O<sub>3</sub>, demonstrating that the obtained product was only composed of ZnFe<sub>2</sub>O<sub>4</sub>-MM and RGO. The average particle size of the prepared ZnFe<sub>2</sub>O<sub>4</sub>-MM was calculated to be ca. 50 nm based on Scherrer's equation [39].

Fig. 1b shows a comparison of the Raman spectra of the ZnFe<sub>2</sub>O<sub>4</sub>-MM, ZnFe<sub>2</sub>O<sub>4</sub>-MM/GO and ZnFe<sub>2</sub>O<sub>4</sub>-MM/RGO hybrid. Well-resolved Raman scattering peaks of ZnFe<sub>2</sub>O<sub>4</sub>-MM are observed at 338, 490, 645 and 1089 cm<sup>-1</sup>, which can be ascribed to the vibration of cubic spinel ZnFe<sub>2</sub>O<sub>4</sub> [40]. Two new peaks of D and G bands from GO are observed at 1357 and 1606 cm<sup>-1</sup> in the Raman spectrum of ZnFe<sub>2</sub>O<sub>4</sub>-MM/GO, where the G band arises from the E<sub>2g</sub> phonon of sp<sup>2</sup>C atoms and the D band is a breathing mode of k-point phonons of A<sub>1g</sub> symmetry [41]. Upon reduction of GO, the G band shifts to a lower value of 1579 cm<sup>-1</sup> (inset of Fig. 1b), and the intensity ratio ( $I_D/I_G$ ) for the ZnFe<sub>2</sub>O<sub>4</sub>-MM/RGO (1.07) is higher than that for ZnFe<sub>2</sub>O<sub>4</sub>-MM/GO (0.86), indicating more graphene domains formed on RGO sheets during reduction process, which led to smaller RGO but more numerous in numbers of sheets [42], thus, facilitating the charge transfer. The results further confirm the co-existence of ZnFe<sub>2</sub>O<sub>4</sub>-MM and RGO sheets.

Furthermore, FTIR spectra are employed to verify the hybridization of ZnFe<sub>2</sub>O<sub>4</sub>-MM with RGO in the hybrid. For pure ZnFe<sub>2</sub>O<sub>4</sub>-MM (Fig. 1c), the bands at 3430 and 563 cm<sup>-1</sup> can be assigned to the stretching vibration mode of hydrogen-bonded surface water molecules and Fe–O functional group, respectively, which is similar to that of reported ZnFe<sub>2</sub>O<sub>4</sub> [21]. Compared with ZnFe<sub>2</sub>O<sub>4</sub>-MM/GO, almost all the characteristic bands of GO were disappeared after the reduction reaction, including OH deformation vibrations of tertiary CO–H (1386 cm<sup>-1</sup>) and C–O stretching vibrations of epoxy groups (1048 cm<sup>-1</sup>), indicating that the oxygen-containing functional groups of GO had been removed from the hybrid [43]. The residual absorption bands at 2975 and 2891 cm<sup>-1</sup> can be assigned to the asymmetric and symmetric vibrations of C–H, respectively, and another peak at 1637 cm<sup>-1</sup> can be attributed to the stretching vibration of C=C of RGO. It showed that the reduction of GO to RGO was completed by a hydrothermal treatment, which can be further supported by XPS observations. Besides, in the hybrid, the stretching vibration of the Fe–O group exhibited a slight-shift toward high wavenumber compared with that of ZnFe<sub>2</sub>O<sub>4</sub>-MM, suggesting that the hybridization may occur between ZnFe<sub>2</sub>O<sub>4</sub>-MM and RGO sheets [44].

Nitrogen adsorption–desorption isotherm measurements are performed to characterize the specific surface areas of ZnFe<sub>2</sub>O<sub>4</sub>-MM and ZnFe<sub>2</sub>O<sub>4</sub>-MM/RGO hybrid (Fig. 1d). Both of them exhibited typical type III isotherm curves caused by the weak adsorbent–adsorbent interaction [45], indicating the presence of porous structures. The measured BET specific surface area of the hybrid is about 26.35 m<sup>2</sup> g<sup>-1</sup>, which is much larger than that of

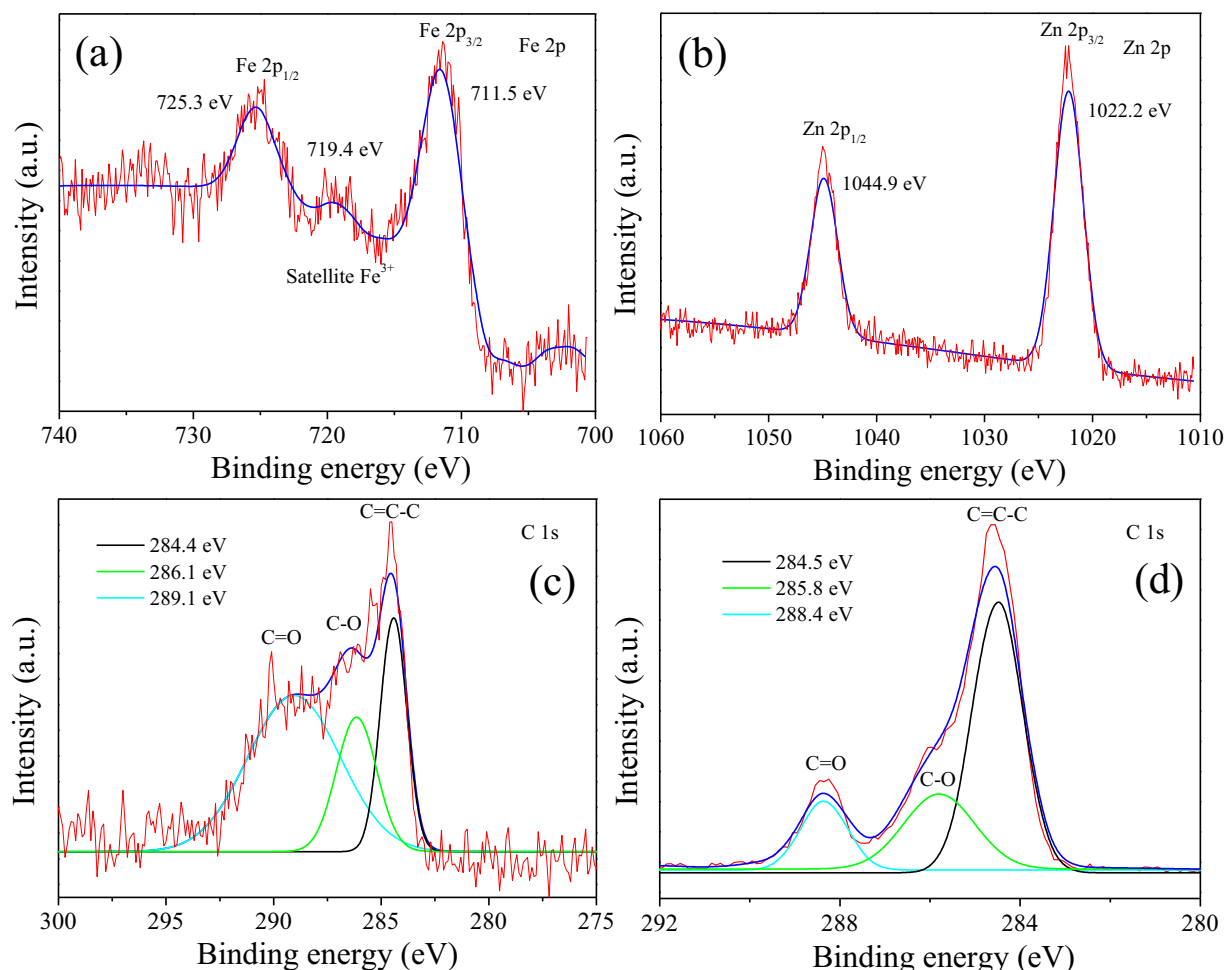


**Fig. 2.** (a) Fe 2p XPS spectrum and (b) Zn 2p XPS spectrum of  $\text{ZnFe}_2\text{O}_4$ -MM/RGO hybrid; the C 1s XPS spectra of  $\text{ZnFe}_2\text{O}_4$ -MM/GO (c) and  $\text{ZnFe}_2\text{O}_4$ -MM/RGO hybrid (d).

pure  $\text{ZnFe}_2\text{O}_4$ -MM ( $11.51 \text{ m}^2 \text{ g}^{-1}$ ) and  $\text{ZnFe}_2\text{O}_4$ -NP ( $3.30 \text{ m}^2 \text{ g}^{-1}$ ), respectively. The increased specific surface area of hybrid was attributed to the introduction of RGO sheets, which could significantly increase the specific surface area of  $\text{ZnFe}_2\text{O}_4$ -MM as expected. Also, the unique brick-like multi-porous structure may provide more active sites for absorption of 4-CP molecules than that of  $\text{ZnFe}_2\text{O}_4$ -NP, resulting in an enhanced photocatalytic activity (indicated later).

To further investigate the elemental composition and chemical state of the  $\text{ZnFe}_2\text{O}_4$ -MM/RGO hybrid, we carried out XPS measurements. The survey XPS spectrum of the  $\text{ZnFe}_2\text{O}_4$ -MM/RGO hybrid revealed the predominant presence of Zn, Fe, O and C elements, and no other hetero-elements were detected (Fig. S1). In Fig. 2a, two distinct peaks at 711.5 eV for Fe  $2p_{3/2}$  and 725.3 eV for Fe  $2p_{1/2}$  with a shake-up satellite at 719.4 eV are observed. This is characteristic of  $\text{Fe}^{3+}$  in the hybrid [46]. For Zn 2p, two peaks at 1044.9 and 1022.2 eV could be assigned to the spectra of Zn  $2p_{1/2}$  and Zn  $2p_{3/2}$  of  $\text{Zn}^{2+}$ , respectively (Fig. 2b), which provide the evidence for existence of  $\text{ZnFe}_2\text{O}_4$  in the hybrid. Similar results were also reported by previous research [39]. Fig. 2c shows the C 1s peaks of  $\text{ZnFe}_2\text{O}_4$ -MM/GO, which can be divided into three main peaks centered at 284.4, 286.1 and 289.1 eV, originated from the C=C–C (sp<sup>2</sup>C and sp<sup>3</sup>C atoms), C–O–H (epoxy and alkoxy) and O–C=O (carboxyl groups), respectively [47]. For hybrid (Fig. 2d), the intensities of all C 1s peaks of the carbon binding to oxygen decrease dramatically, revealing that most oxygen containing functional groups are removed after the hydrothermal treatment. This result is consistent with the FTIR and Raman analysis.

Fig. 3a–e shows the FESEM images of  $\text{ZnFe}_2\text{O}_4$ -MM and  $\text{ZnFe}_2\text{O}_4$ -MM/RGO hybrid. A panoramic view shows that the  $\text{ZnFe}_2\text{O}_4$ -MM consists entirely of uniform microbricks with an average edge length of around  $8 \mu\text{m}$  (Fig. 3a). The high magnification FESEM images in Fig. 3b and c shows that these microbricks have multi-porous structures with a rough surface. Fortunately, the hollow interior can be directly observed through some openings on the  $\text{ZnFe}_2\text{O}_4$ -MM surfaces during the FESEM observation (Fig. 3c), indicating that the existence of quasi-hollow structures in the multi-porous microbricks. The quasi-hollow structure allows the entrance and multiple reflection of light in the interior cavity, resulting in more efficient use of the light source [48,49]. Moreover, the robust structure and rough surface of  $\text{ZnFe}_2\text{O}_4$ -MM provide the feasibility of exploiting coating of RGO sheets around the bricks. Note that successful exfoliation of the graphite is evidenced by TEM images of individual sheets resembling slightly crumpled paper (inset of Fig. 3i). FESEM examinations show that after RGO sheets coating, there is no apparent change in the morphology of the microbricks although the RGO sheets and the  $\text{ZnFe}_2\text{O}_4$ -MM are intimately intermixed and can be made out clearly (Fig. 3d and e). The corresponding EDX measurement further confirms the co-existence of Zn, Fe, O, C and Si elements (Fig. 3f). The quantitative analysis reveals that the atomic ratio of Zn and Fe in the hybrid is close to 1:2, which is consistent with the stoichiometric composition of  $\text{ZnFe}_2\text{O}_4$ . Note that the silicon signal originates from the underlying support.

Further information about the microstructure of the samples is obtained from TEM images. Enlarged TEM images of  $\text{ZnFe}_2\text{O}_4$ -MM



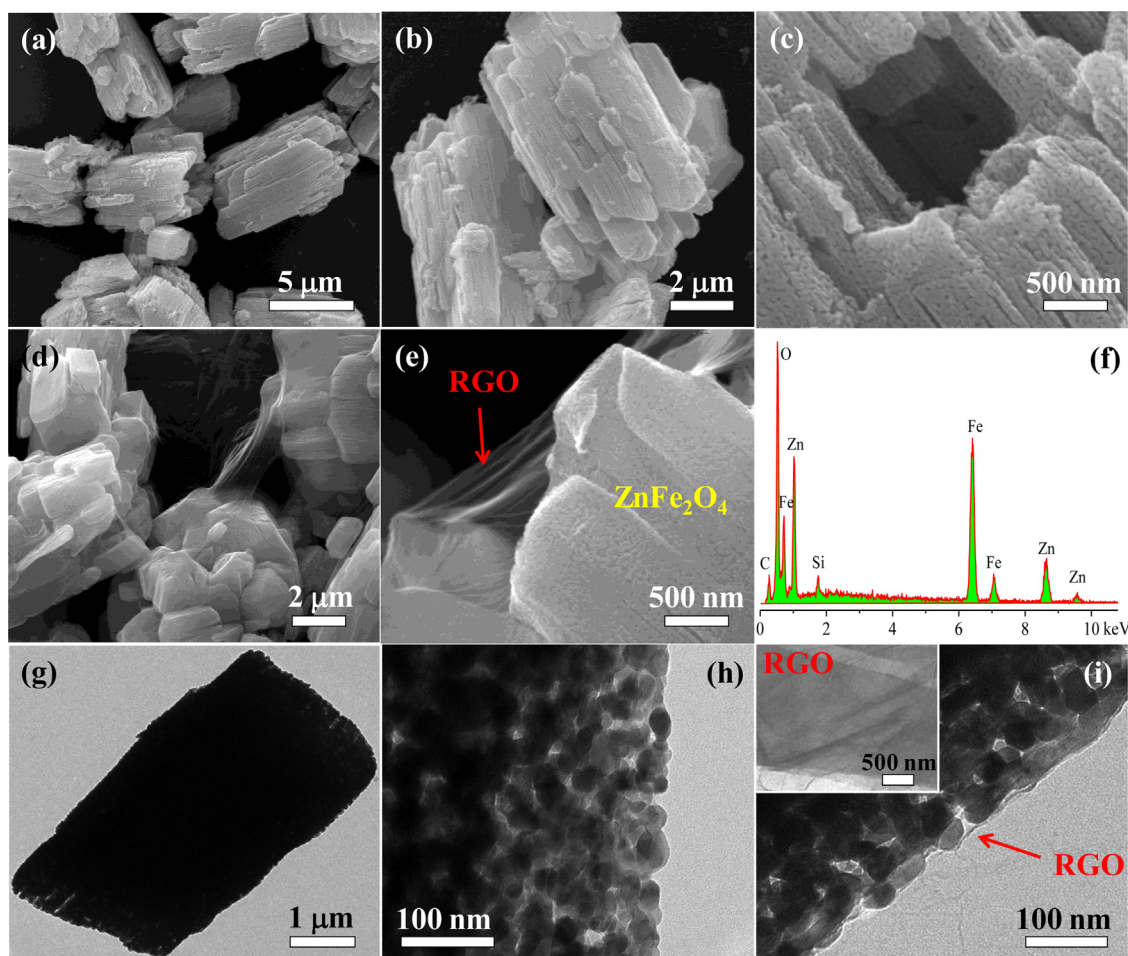


**Fig. 3.** FESEM images of the ZnFe<sub>2</sub>O<sub>4</sub>-MM (a–c) and ZnFe<sub>2</sub>O<sub>4</sub>-MM/RGO hybrid (d–e). The corresponding EDX spectrum of the hybrid is shown in (f). TEM images of the ZnFe<sub>2</sub>O<sub>4</sub>-MM (g–h) and ZnFe<sub>2</sub>O<sub>4</sub>-MM/RGO hybrid (i). Inset is the TEM image of RGO sheets.

(Fig. 3g and h) show that the multi-porous microbrick is formed through the agglomeration of numerous small nanoparticles with diameters of about 40 nm. Compared with the ZnFe<sub>2</sub>O<sub>4</sub>-MM, the ZnFe<sub>2</sub>O<sub>4</sub>-MM/RGO displays a good combination between ZnFe<sub>2</sub>O<sub>4</sub>-MM and RGO sheets; the multi-porous microbrick is tightly wrapped by the RGO sheets (Fig. 3i). This unique structure feature is beneficial for the separation of photo-generated electrons and holes, and further enhances its photocatalytic activity.

TGA analysis is employed to determine the amount of RGO present in ZnFe<sub>2</sub>O<sub>4</sub>-MM/RGO. As shown in Fig. 4a, a large weight loss occurred at 400–600 °C, which was ascribed to the decomposition of the RGO sheets [50]. The remaining materials were quite stable without further weight loss above 700 °C. Assuming that the final residue was only ZnFe<sub>2</sub>O<sub>4</sub>-MM, we calculated that the amount of RGO in the hybrid was about 14.9%. This value was close to the expected value of 12.5% based on amounts of GO (20 mg) used and ZnFe<sub>2</sub>O<sub>4</sub>-MM/RGO (0.16 g) obtained.

Fig. 4b displays the UV–vis absorption spectra of the ZnFe<sub>2</sub>O<sub>4</sub>-NP, ZnFe<sub>2</sub>O<sub>4</sub>-MM and ZnFe<sub>2</sub>O<sub>4</sub>-MM/RGO. It can be seen that pure ZnFe<sub>2</sub>O<sub>4</sub>-MM exhibited strong photo-absorption from the UV to visible light region shorter than 625 nm. Compared with the ZnFe<sub>2</sub>O<sub>4</sub>-MM, the absorption edge of ZnFe<sub>2</sub>O<sub>4</sub>-MM/RGO exhibited slight red-shift to higher wavelength and the absorption intensity significantly increased both in the UV and visible light regions, which resulted from the loading of RGO sheets. The presence of RGO induced a continuous absorption band in the range of 650–800 nm and the strong absorption intensity in the hybrid due to the reducing reflection of light [51]. Besides, the red-shift result indicated

that the narrowing of the band-gap of the ZnFe<sub>2</sub>O<sub>4</sub>-MM occurred upon the RGO introduction. This narrowing may be attributed to the formation of Fe–O–C chemical bonds between ZnFe<sub>2</sub>O<sub>4</sub>-MM and RGO [29]. The results agree well with the results from FTIR measurement.

A plot of the transformed Kubelka–Munk function as a function of energy of light is shown in Fig. 4c, from which the estimated band-gap values are 1.97 and 1.92 eV corresponding to the ZnFe<sub>2</sub>O<sub>4</sub>-MM and ZnFe<sub>2</sub>O<sub>4</sub>-MM/RGO, respectively [14], which are smaller than that of ZnFe<sub>2</sub>O<sub>4</sub>-NP (2.08 eV). The right-shifts might be ascribed to the additional sub-band-gap energy levels induced by the abundant surface and interface defects in the agglomerated nanoparticles [52], which will enhance the light harvesting efficiency. Improved photocatalytic activity of the hybrid is expected.

Moreover, a drastic quenching of photoluminescence intensity of ZnFe<sub>2</sub>O<sub>4</sub>-MM was observed after the introduction of RGO sheets (Fig. 4d), indicating that the recombination of the photo-generated charge carriers was greatly reduced in the hybrid. This phenomenon suggested that the RGO sheets loaded on ZnFe<sub>2</sub>O<sub>4</sub>-MM could act as traps to capture the photoinduced electrons from ZnFe<sub>2</sub>O<sub>4</sub>-MM, leading to the spatial separation of the photoinduced electron–hole pairs due to the excellent electronic conductivity of RGO sheets [26].

### 3.2. Photocatalytic degradation 4-CP

To investigate the photocatalytic activity of the ZnFe<sub>2</sub>O<sub>4</sub>-MM/RGO hybrid, several photocatalytic experiments were carried

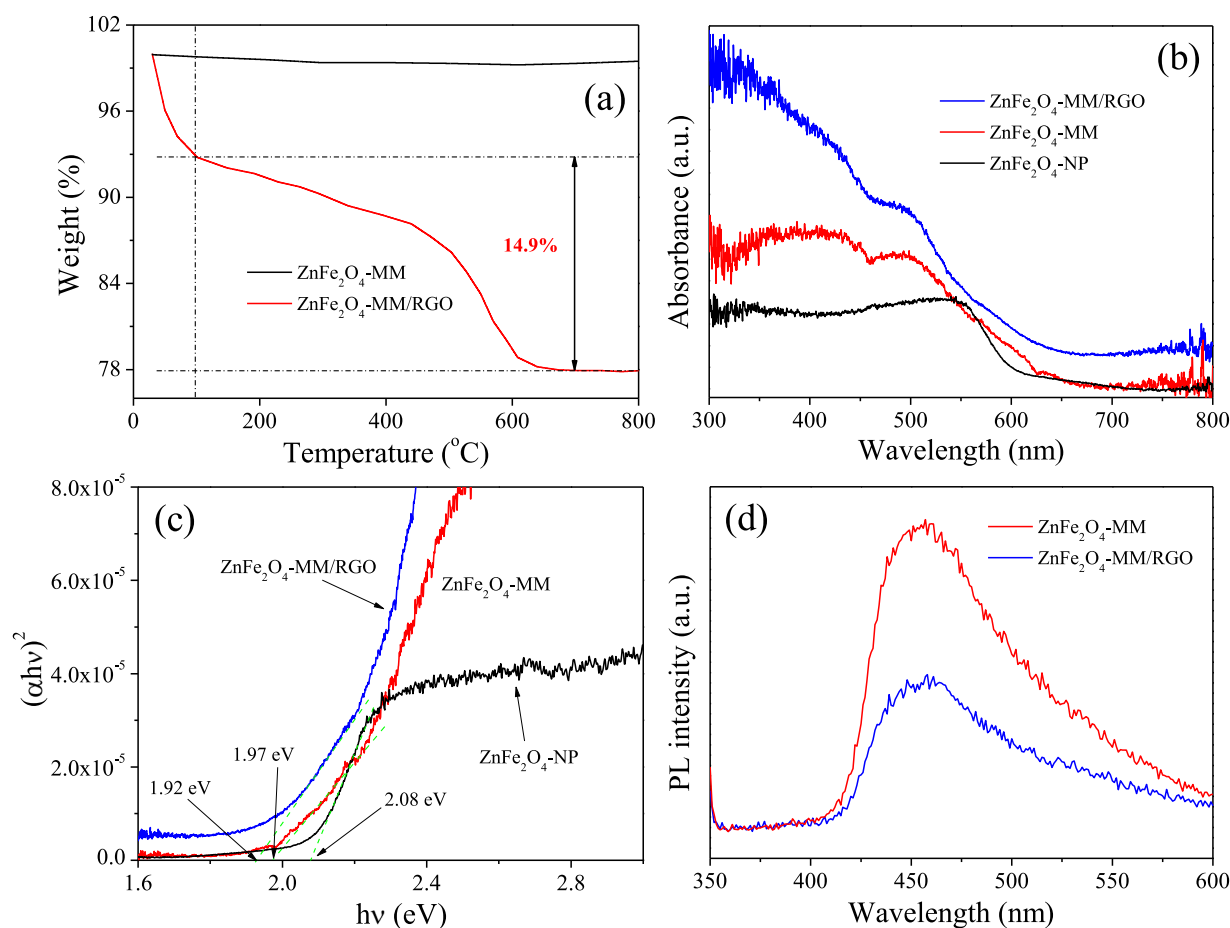


**Fig. 4.** (a) TGA curves of ZnFe<sub>2</sub>O<sub>4</sub>-MM and ZnFe<sub>2</sub>O<sub>4</sub>-MM/RGO. The weight loss at the temperature below 100 °C is attributed to the evaporation of moisture. UV–vis absorption spectra (b), the corresponding plots of  $(\alpha h\nu)^2$  vs. photon energy ( $h\nu$ ) (c) and PL spectra (d) of the ZnFe<sub>2</sub>O<sub>4</sub>-MM and ZnFe<sub>2</sub>O<sub>4</sub>-MM/RGO hybrid. Additionally, data for ZnFe<sub>2</sub>O<sub>4</sub>-NP are also shown.

out for 4-CP degradation under visible light irradiation ( $\lambda > 420$  nm,  $I_0 = 71.4 \text{ mW cm}^{-2}$ ). As shown in Fig. 5a, the direct photolysis of 4-CP without any photocatalysts was almost absent because 4-CP was very stable in this process. The removal efficiency was enhanced to 50.5% when ZnFe<sub>2</sub>O<sub>4</sub>-NP was added after 120 min. However, it was enhanced to 91.4% when the same amount of ZnFe<sub>2</sub>O<sub>4</sub>-MM was added as photocatalyst. In contrast, ZnFe<sub>2</sub>O<sub>4</sub>-MM/RGO hybrid exhibited the highest photocatalytic activity for degradation of 4-CP and a complete removal of 4-CP was observed after only 60 min irradiation. Provided that the photocatalytic reaction follows a pseudo-first-order reaction (Fig. 5b), the kinetic constant over ZnFe<sub>2</sub>O<sub>4</sub>-MM/RGO hybrid ( $0.0459 \text{ min}^{-1}$ ) was about 2.08 and 7.29 times higher than that of ZnFe<sub>2</sub>O<sub>4</sub>-MM ( $0.0221 \text{ min}^{-1}$ ) and ZnFe<sub>2</sub>O<sub>4</sub>-NP ( $0.0063 \text{ min}^{-1}$ ), respectively. Such an enhancement is mainly attributed to the improved light absorption, large specific surface area of microbricks and the modification of RGO sheets. The RGO sheets could serve as an excellent acceptor of the electrons photogenerated from the ZnFe<sub>2</sub>O<sub>4</sub>-MM and effectively decrease the recombination probability of the photoexcited electron–hole pairs, leaving more charge carriers participated in the photocatalytic reaction.

To further investigate the photocatalytic activity of ZnFe<sub>2</sub>O<sub>4</sub>-MM/RGO hybrid, the TOC experiment is performed, shown in Fig. 5c. The results showed that the rate of TOC reduction was remarkably slower than that of 4-CP. About 54.77% of TOC still remained in the suspension after 60 min irradiation while 4-CP was completely degraded. Such results did not surprise us. Like other

organic compounds, 4-CP required a longer irradiation time for total mineralization than for the corresponding degradation [53].

Fig. 5d shows the time profile of five repeated experiments of 4-CP photocatalytic degradation, using the ZnFe<sub>2</sub>O<sub>4</sub>-MM/RGO hybrid under the same experimental conditions. The results clearly showed a good reproducibility with the degradation rate of 82.8% retained even after five repeated experiments. Moreover, the XPS survey spectra of the hybrid before and after experiments were almost identical, which further support the above results (Fig. S1).

### 3.3. Hydroxyl radical analysis

To understand the active species involved in the photocatalytic process, we employed the PL technique using terephthalic acid as a probe to investigate the generation of  $\cdot\text{OH}$  [54]. Fig. 6a shows the changes of PL spectra from  $5 \times 10^{-1} \text{ M}$  terephthalic acid solution in  $2 \times 10^{-1} \text{ M}$  NaOH with irradiation time. A gradual increase in PL intensity at about 425 nm was observed with increasing irradiation time for ZnFe<sub>2</sub>O<sub>4</sub>-MM/RGO hybrid, which indicated the production of  $\cdot\text{OH}$  radicals. Additionally, we compared the PL intensity for ZnFe<sub>2</sub>O<sub>4</sub>-NP, ZnFe<sub>2</sub>O<sub>4</sub>-MM and ZnFe<sub>2</sub>O<sub>4</sub>-MM/RGO hybrid at 20 min after irradiation (Fig. 6b). The PL intensity of hybrid was much higher than that of the ZnFe<sub>2</sub>O<sub>4</sub>-NP and ZnFe<sub>2</sub>O<sub>4</sub>-MM. Usually, PL intensity was proportional to the amount of produced  $\cdot\text{OH}$  radicals. It could be easily seen that at a fixed time, the amount of  $\cdot\text{OH}$  radicals produced on hybrid was larger than that of  $\cdot\text{OH}$  radicals produced on ZnFe<sub>2</sub>O<sub>4</sub>-MM and ZnFe<sub>2</sub>O<sub>4</sub>-NP, respectively,

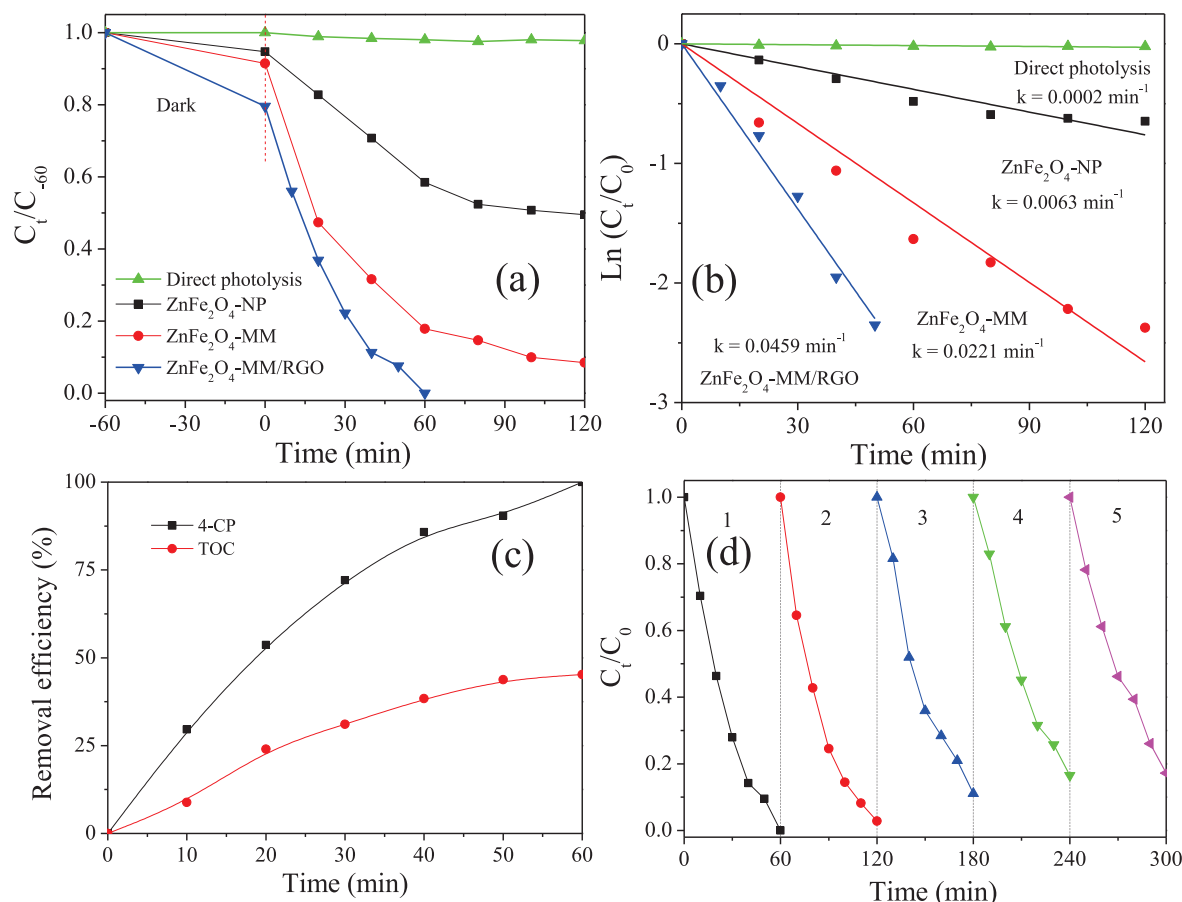


**Fig. 5.** (a) The processes of photocatalytic degradation of 4-CP under visible light irradiation ( $\lambda > 420 \text{ nm}$ ) and (b) the variation of  $\ln(C/C_0)$  of 4-CP by different processing routes. (c) 4-CP and TOC removal during the course of the photocatalytic degradation with  $ZnFe_2O_4$ -MM/RGO hybrid. (d) Cyclic photodegradation of 4-CP by the  $ZnFe_2O_4$ -MM/RGO hybrid for five times.

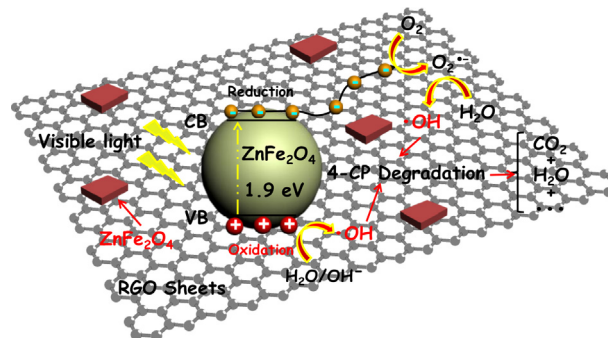
indicating that the higher photocatalytic activity could be obtained by hybrid. Also, the above results show that the  $\bullet\text{OH}$  radicals are the main active species in the photocatalytic process of the 4-CP/ $ZnFe_2O_4$ -MM/RGO hybrid system.

To further confirm this result, the radicals and holes trapping experiments were designed to elucidate the photocatalytic degradation of 4-CP process over  $ZnFe_2O_4$ -MM/RGO hybrid. As shown in Fig. 7, the photocatalytic degradation of 4-CP was slightly retarded with about 7.73% reduction by the injection of a scavenger for holes (EDTA) [55], which implied the minor role of holes either acting as the oxidizing agent or the origination of the  $\bullet\text{OH}$  radicals in this process. With the addition of tBuOH [56], an efficient  $\bullet\text{OH}$  radicals quencher, the degradation efficiency of 4-CP was depressed markedly and only 27.22% of the 4-CP was degraded after 60 min irradiation, indicating  $\bullet\text{OH}$  radicals was the primary oxidant in the photocatalytic reaction. Meanwhile,  $\text{O}_2^{\bullet-}$  may also serve as active species in this reaction because the degradation of 4-CP was inhibited by  $\text{N}_2$  bubbling [54]. These results further confirmed that  $\bullet\text{OH}$  radicals were the primary active species in this system, while both holes and  $\text{O}_2^{\bullet-}$  were also involved.

#### 3.4. Photocatalytic mechanism discussion

Based on the characterization of structure and properties, a plausible reaction mechanism for the high photocatalytic activity of  $ZnFe_2O_4$ -MM/RGO hybrid was proposed as illustrated in Scheme 1. Under visible light irradiation ( $\lambda > 420 \text{ nm}$ ),  $ZnFe_2O_4$ -MM absorbed visible light and was excited. The photogenerated

electrons were migrated from the valence band (VB) of  $ZnFe_2O_4$ -MM to the conduction band (CB), leaving the holes in the VB of  $ZnFe_2O_4$ -MM. Owing to the well-matched band potential between  $ZnFe_2O_4$  and RGO [15,27], the photogenerated electrons accumulated on the CB of  $ZnFe_2O_4$ -MM then tended to transfer to RGO sheets, and thus the probability of electron–hole recombination was effectively suppressed. In this process, RGO sheets can function as an electron collector and transporter to lengthen the lifetime of the charge carriers, improving the whole photocatalytic activity [57]. The leftover holes directly react with 4-CP or interact with surface-bound  $\text{H}_2\text{O}$  or  $\text{OH}^-$  to produce the  $\bullet\text{OH}$  radical species which is an extremely strong oxidant for the



**Scheme 1.** Possible mechanism of the photocatalytic degradation of 4-CP over  $ZnFe_2O_4$ -MM/RGO hybrid under visible light irradiation ( $\lambda > 420 \text{ nm}$ ).

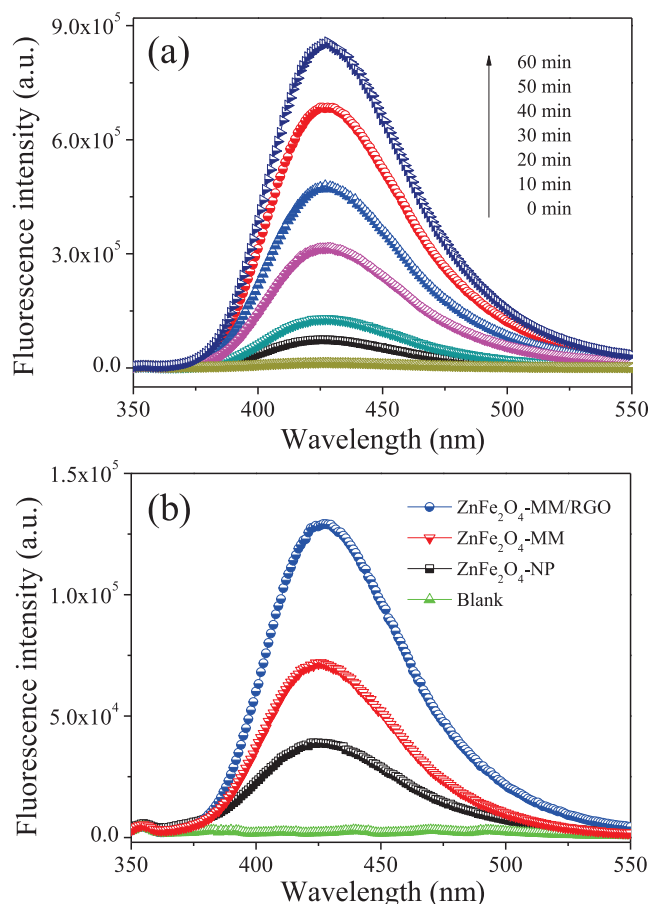


**Fig. 6.** (a) PL spectral changes with irradiation time on ZnFe<sub>2</sub>O<sub>4</sub>-MM/RGO hybrid in a 5 × 10<sup>-4</sup> M basic solution of terephthalic acid and (b) PL spectra of ZnFe<sub>2</sub>O<sub>4</sub>-NP, ZnFe<sub>2</sub>O<sub>4</sub>-MM and ZnFe<sub>2</sub>O<sub>4</sub>-MM/RGO hybrid in a 5 × 10<sup>-4</sup> M basic solution of terephthalic acid under visible light irradiation (λ > 420 nm) at a fixed 20 min.

mineralization of 4-CP. Meanwhile, the electrons formed can react with the adsorbed molecular oxygen to yield O<sub>2</sub><sup>•-</sup>. The generated O<sub>2</sub><sup>•-</sup> then further combine with H<sup>+</sup> to produce generate •OH radicals [58]. All the reactive species, such as •OH, O<sub>2</sub><sup>•-</sup> and holes, could oxidize 4-CP to CO<sub>2</sub>, H<sub>2</sub>O or other intermediates to some degree.

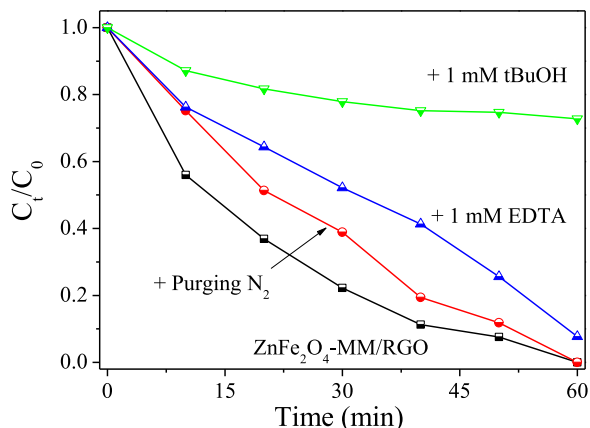


**Fig. 7.** Plots of photogenerated carriers trapping in the system of photocatalytic degradation of 4-CP over ZnFe<sub>2</sub>O<sub>4</sub>-MM/RGO hybrid (□), ZnFe<sub>2</sub>O<sub>4</sub>-MM/RGO hybrid/Purging N<sub>2</sub> (○), ZnFe<sub>2</sub>O<sub>4</sub>-MM/RGO hybrid/1 mM EDTA (△) and ZnFe<sub>2</sub>O<sub>4</sub>-MM/RGO hybrid/1 mM tBuOH (▽) under visible light irradiation (λ > 420 nm).

## 4. Conclusions

In summary, a hybrid photocatalyst of ZnFe<sub>2</sub>O<sub>4</sub>-MM/RGO was successfully prepared by a facile two-step strategy, which exhibited enhanced photocatalytic activity in the degradation of 4-CP under visible light irradiation (λ > 420 nm). The kinetic constant of 4-CP removal with ZnFe<sub>2</sub>O<sub>4</sub>-MM/RGO hybrid was about 2.08 and 7.29 times higher than that of pure ZnFe<sub>2</sub>O<sub>4</sub>-MM and ZnFe<sub>2</sub>O<sub>4</sub>-NP, respectively. We attributed this improvement to the integrative effect of the enhanced light absorption, unique morphology and structure, and facilitated separation of photogenerated carriers owing to the synergetic interaction between ZnFe<sub>2</sub>O<sub>4</sub>-MM and RGO, the latter evidenced by PL analyses. It is believed that the present approach for the hybrid photocatalyst preparation and the detailed mechanism discussion in this work can provide valuable knowledge on the development of graphene-based highly efficient photocatalysts for environmental remediation technology. Also, the synthesis method may be useful for constructing other graphene-based hybrids.

## Acknowledgements

This work was supported financially by the National Nature Science Foundation of China (NSFC-RGC 21061160495), the National High Technology Research and Development Program of China (863 Program) (No. 2010AA064902) and the Key Laboratory of Industrial Ecology and Environmental Engineering, China Ministry of Education.

## Appendix A. Supplementary data

Supplementary data associated with this article can be found, in the online version, at <http://dx.doi.org/10.1016/j.apcatb.2013.04.062>.

## References

- [1] X. Chen, S.S. Mao, Chemical Reviews 107 (2007) 2891–2959.
- [2] H. Zhou, Y. Qu, T. Zeid, X. Duan, Energy & Environmental Science 5 (2012) 6732–6743.
- [3] A. Fujishima, K. Honda, Nature 238 (1972) 37–38.
- [4] A.L. Linsebigler, G.Q. Lu, J.T. Yates, Chemical Reviews 95 (1995) 735–758.
- [5] I.S. Cho, Z. Chen, A.J. Forman, D.R. Kim, P.M. Rao, T.F. Jaramillo, X. Zheng, Nano Letters 11 (2011) 4978–4984.
- [6] L. Peng, T. Xie, Y. Lu, H. Fan, D. Wang, Physical Chemistry Chemical Physics 12 (2010) 8033–8041.
- [7] C.H. Kim, Y. Myung, Y.J. Cho, H.S. Kim, S.H. Park, J. Park, J.Y. Kim, B. Kim, Journal of Physical Chemistry C 113 (2009) 7085–7090.
- [8] Z. Zhou, Y. Zhang, Z. Wang, W. Wei, W. Tang, J. Shi, R. Xiong, Applied Surface Science 254 (2008) 6972–6975.
- [9] S. Xuan, F. Wang, J.M.Y. Lai, K.W.Y. Sham, Y.X.J. Wang, S.F. Lee, J.C. Yu, C.H.K. Cheng, K.C.F. Leung, ACS Applied Materials & Interfaces 3 (2011) 237–244.
- [10] W. Pon-On, N. Charoenphandhu, I.M. Tang, P. Jongwattanasapian, N. Krishnamra, R. Hoonsawat, Materials Chemistry and Physics 131 (2011) 485–494.
- [11] F. Liu, X. Li, Q. Zhao, Y. Hou, X. Quan, G. Chen, Acta Materialia 57 (2009) 2684–2690.
- [12] H. Lv, L. Ma, P. Zeng, D. Ke, T. Peng, Journal of Materials Chemistry 20 (2010) 3665–3672.
- [13] P.P. Hankare, R.P. Patil, A.V. Jadhav, K.M. Garadkar, R. Sasikala, Applied Catalysis B 107 (2011) 333–339.
- [14] X. Li, Y. Hou, Q. Zhao, L. Wang, Journal of Colloid and Interface Science 358 (2011) 102–108.
- [15] X. Liu, H. Zheng, Y. Li, W. Zhang, Journal of Materials Chemistry C 1 (2013) 329–337.
- [16] X. Li, Y. Hou, Q. Zhao, W. Teng, X. Hu, G. Chen, Chemosphere 82 (2011) 581–586.
- [17] M.M. Rahman, S.B. Khan, M. Faisal, A.M. Asiri, K.A. Alamry, Sensors and Actuators B 171–172 (2012) 932–937.
- [18] P.F. Teh, Y. Sharma, S.S. Pramana, M. Srinivasan, Journal of Materials Chemistry 21 (2011) 14999–15008.
- [19] M. Arias, V.M. Pantojas, O. Perales, W. Otaño, Journal of Magnetism and Magnetic Materials 323 (2011) 2109–2114.
- [20] M. Wang, Z.H. Ai, L.Z. Zhang, Journal of Physical Chemistry C 112 (2008) 13163–13170.



- [21] M. Wang, Z. Ai, L. Zhang, *Journal of Physical Chemistry C* 112 (2008) 13163–13170.
- [22] Y. Deng, Q. Zhang, S. Tang, L. Zhang, S. Deng, Z. Shi, G. Chen, *Chemical Communications* 47 (2011) 6828–6830.
- [23] Y. Shen, X. Li, Q. Zhao, Y. Hou, M. Tade, S. Liu, *Materials Research Bulletin* 46 (2011) 2235–2239.
- [24] K.S. Novoselov, A.K. Geim, S.V. Morozov, D. Jiang, Y. Zhang, S.V. Dubonos, I.V. Grigorieva, A.A. Firsov, *Science* 306 (2004) 666–669.
- [25] S. Guo, S. Dong, *Chemical Society Reviews* 40 (2011) 2644–2672.
- [26] A.K. Geim, *Science* 324 (2009) 1530–1534.
- [27] Y. Fu, X. Wang, *Industrial and Engineering Chemistry Research* 50 (2011) 7210–7218.
- [28] X. Chen, B. Cheng, H. Xu, J. Yang, Y. Qian, *Chemistry Letters* 41 (2012) 639–641.
- [29] W. Song, J. Xie, S. Liu, G. Cao, T. Zhu, X. Zhao, *New Journal of Chemistry* 36 (2012) 2236–2241.
- [30] W.S. Hummers, R.E. Offeman, *Journal of the American Chemical Society* 80 (1958) 1339.
- [31] Sirajuddin, M.I. Bhanger, A. Niaz, A. Shah, A. Rauf, *Talanta* 72 (2007) 546–553.
- [32] A. Dhir, N.T. Prakash, D. Sud, *Desalination and Water Treatment* 46 (2012) 196–204.
- [33] B. Philipp, B. Schink, *Journal of Bacteriology* 180 (1998) 3644–3649.
- [34] J. Kunczewicz, P. Ząbek, K. Kruczała, K. Szaciłowski, W. Macyk, *Journal of Physical Chemistry C* 116 (2012) 21762–21770.
- [35] B. Gao, Y.J. Kim, A.K. Chakraborty, W.I. Lee, *Applied Catalysis B* 83 (2008) 202–207.
- [36] A. Zaleska, P. Górka, J.W. Sobczak, J. Hupka, *Applied Catalysis B* 76 (2007) 1–8.
- [37] K.I. Ishibashi, A. Fujishima, T. Watanabe, K. Hashimoto, *Electrochemistry Communications* 2 (2000) 207–210.
- [38] P. Wang, J. Wang, X. Wang, H. Yu, J. Yu, M. Lei, Y. Wang, *Applied Catalysis B* 132–133 (2013) 452–459.
- [39] Y. Hou, X.Y. Li, Q.D. Zhao, X. Quan, G.H. Chen, *Advanced Functional Materials* 20 (2010) 2165–2174.
- [40] M.H. Sousa, F.A. Tourinho, J.C. Rubim, *Journal of Raman Spectroscopy* 31 (2000) 185–191.
- [41] Y. Hou, F. Zuo, A. Dagg, P. Feng, *Nano Letters* 12 (2012) 6464–6473.
- [42] Y. Liu, Y. Hu, M. Zhou, H. Qian, X. Hu, *Applied Catalysis B* 125 (2012) 425–431.
- [43] A. Cao, Z. Liu, S. Chu, M. Wu, Z. Ye, Z. Cai, Y. Chang, S. Wang, Q. Gong, Y. Liu, *Advanced Materials* 22 (2010) 103–106.
- [44] Q. Liang, Y. Shi, W. Ma, Z. Li, X. Yang, *Physical Chemistry Chemical Physics* 14 (2012) 15657–15665.
- [45] H. Ma, J. Shen, M. Shi, X. Lu, Z. Li, Y. Long, N. Li, M. Ye, *Applied Catalysis B* 121–122 (2012) 198–205.
- [46] Y. Hou, F. Zuo, A. Dagg, P. Feng, *Angewandte Chemie International Edition* 52 (2013) 1248–1252.
- [47] D. Zhao, G. Sheng, C. Chen, X. Wang, *Applied Catalysis B* 111–112 (2012) 303–308.
- [48] H. Li, Z. Bian, J. Zhu, D. Zhang, G. Li, Y. Huo, H. Li, Y. Lu, *Journal of the American Chemical Society* 129 (2007) 8406–8407.
- [49] J. Zhuang, Q. Tian, H. Zhou, Q. Liu, P. Liu, H. Zhong, *Journal of Materials Chemistry* 22 (2012) 7036–7042.
- [50] Y. Zou, Y. Wang, *Nanoscale* 3 (2011) 2615–2620.
- [51] L. Jia, D.H. Wang, Y.X. Huang, A.W. Xu, H.Q. Yu, *Journal of Physical Chemistry C* 115 (2011) 11466–11473.
- [52] N. Kislov, S.S. Srinivasan, Y. Emirov, E.K. Stefanakos, *Materials Science and Engineering B* 153 (2008) 70–77.
- [53] Y. Hou, X. Li, Q. Zhao, X. Quan, G. Chen, *Environmental Science and Technology* 44 (2010) 5098–5103.
- [54] W. Teng, X.Y. Li, Q.D. Zhao, J.J. Zhao, D.K. Zhang, *Applied Catalysis B* 125 (2012) 538–545.
- [55] C. Pan, Y. Zhu, *Environmental Science and Technology* 44 (2010) 5570–5574.
- [56] M. Yin, Z. Li, J. Kou, Z. Zou, *Environmental Science and Technology* 43 (2009) 8361–8366.
- [57] Q. Xiang, J. Yu, M. Jaroniec, *Chemical Society Reviews* 41 (2012) 782–796.
- [58] S. Kaneco, M.A. Rahman, T. Suzuki, H. Katsumata, K. Ohta, *Journal of Photochemistry and Photobiology A* 163 (2004) 419–424.